Compact optical fiber sensor based on Vernier effect with speckle patterns

FANG ZHAO,[1] **WEIHAO LIN,**[1,2] **PENGLAI GUO,**[3] **JIE HU,**[1]
YUHUI LIU,[4] **SHUAIQI LIU,**[1,2] **FEIHONG YU,**[1] **GUOMENG ZUO,**[1,5]
GUOQING WANG,[6] **HUANHUAN LIU,**[1] **JINNA CHEN,**[1] **YI LI,**[7]
PERRY PING SHUM,[1,5] **AND LIYANG SHAO**[1,5,*]

[1]*School of Electronic and Electrical Engineering, Southern University of Science and Technology, Shenzhen 518055, China*
[2]*Department of Electrical and Computer Engineering, Faculty of Science and Technology, University of Macau, Macau 999078, China*
[3]*School of Computer Science and Engineering, Macau University of Science and Technology, Macau 999078, China*
[4]*Department of Applied Physics, Hong Kong Polytechnic University, Hongkong 999077, China*
[5]*Peng Cheng Laboratory, Shenzhen 518055, Guangdong, China*
[6]*School of Microelectronics, Shenzhen Institute of Information Technology, Shenzhen 518172, China*
[7]*College of Optical and Electronic Technology, China Jiliang University, Hangzhou 310018, China*
[*]*shaoly@sustech.edu.cn*

Abstract: We propose a Vernier effect-based sensor for temperature and salinity measurements. This sensor utilizes the correlation speckle pattern generated by spatial multimode interference and has undergone testing to validate its effectiveness. The speckle demodulation method is used to solve the problem of inconsistent envelope measurement when tracking with different upper and lower envelopes. The device consists of two Fabry Perot interferometers (FPIs) created by connecting hole core fiber (HCF) and erbium-doped fiber (EDF) in series. The speckle image produced by the interferometers is analyzed using the Zero means normalized cross-correlation (ZNCC) technique. The ZNCC value demonstrates a linear relationship with salinity and temperature, allowing for the measurement of these parameters. The sensor exhibits a temperature detection sensitivity of -0.0224 /°C and a salinity detection sensitivity of -0.0439/%. The sensor offers several advantageous features, including its compact size, low-cost manufacturing, high sensitivity, stability, and convenient reflection measurements. These characteristics make it a valuable tool for various applications. The proposed Vernier effect-based temperature and salinity sensor shows great potential for simultaneous monitoring and measurement of temperature and salinity in environments such as marine settings or industrial processes where accurate control of these parameters is crucial.

1. Introduction

The ocean, accounting for 97% of the earth's total water resources, serves as a vital lifeline for human survival. It plays an indispensable role in driving economic and social development. However, the combined impacts of human activities and global climate change have led to gradual transformations in marine ecosystems. Temperature and salinity are the basic contents of oceanographic research. The distribution and variation of temperature and salinity in the ocean and their relationship with each other are related to ocean thermodynamics and dynamics [1]. Temperature and salinity are critical to our environment, and measuring these parameters to prevent harmful effects on ecosystems is critical. Salinity also plays an important role in the global water cycle, climate variability, and predictability [2].

In recent years, the research of optical fiber sensors has been widely concerned by researchers [3]. Compared with the electronic sensor, it has the advantages of simple manufacture, low cost, light weight, electromagnetic interference resistance, and durability [4]. Furthermore, one of the key advantages of optical fiber sensors is their ability to operate in harsh environments and can be combined with a variety of demodulation schemes [5]. This enables reliable measurement in challenging environments as well as in complex environments such as environmental monitoring, marine settings, and industrial processes [6].

To obtain higher sensor sensitivity, the optical Vernier effect is a promising method to improve the sensitivity and resolution of optical fiber interferometers [7]. Interferometer-based fiber optical sensor structures include the Mach-Zehnder interferometer (MZI), Michelson Interference (MI), Sagnac interferometer, and Fabry Perot interferometer (FPI). It can be obtained by controlling the free spectral range (FSR) of two interferometers in parallel or in series to make them close but not equal to produce the Vernier effect. For example, series MZI and FPI structures [8], cascaded Sagnac loops [9,10], cascade FPI [11], splicing MZI, hybrid cascaded FPI cavity with Sagnac loop [12], MI cascaded FPI [13], etc. Among them, the hybrid structure FPI sensor has been used for temperature and salinity measurement because of its high precision and good resolution. A variety of manufacturing processes have been used for the production of FPI cavities, including the design of a chemical etching process [14], a femtosecond laser writing process [11,15], a splicing process [16], etc. Among them, the splicing process is relatively simple to prepare.

Fiber speckle pattern sensor (FSS), is based on speckle patterns caused by interference between multiple propagation modes in a multimode fiber (MMF) [17]. Previous studies in this area have reported the spatiotemporal properties of speckle patterns used to detect changes in waveguide characteristics, such as temperature [18], stress, refractive index, curvature [19], displacement [20], tactile [21], and other physical quantities. Compared with traditional demodulation methods such as optical spectrum analyzer (OSA), FSS has the advantages of a simple system, low cost, portability, and high sensitivity detection, and has been widely studied by scholars. With the development of charge-coupled device (CCD) camera technology, higher acquisition frequency is obtained [22].

The demodulation method of OSA measures the response of the measured object by observing the spectral changes of the upper envelope or the lower envelope. However, the choice of the envelope will cause uncertainty in the measurement results, and the sensitivity measured by the upper envelope or lower envelope is inconsistent [23]. Therefore, a more accurate and stable Vernier effect demodulation method should be considered to eliminate the uncertainty of measurement results. The speckle pattern intensity is related to the mode coupling and power variations [22]. The demodulation scheme based on speckle patterns can meet the requirements of accurate measuring, high resolution, and high-speed measurement at the same time [24]. Combined with the high sensitivity of the Vernier effect, it can provide a new solution for the development of optical fiber sensors.

This work introduces an optical fiber speckle sensor based on the Vernier effect. The Vernier effect of the sensor is demodulated by analyzing the speckle pattern. The uniqueness of the results of speckle demodulation solves the problem that the measurement results of the upper envelope and the lower envelope are inconsistent during the demodulation of OSA. The sensor is easy to prepare and has a small structure (less than 0.5 mm). Speckles may detect minute changes, and the Vernier effect can increase the sensitivity of the sensor. The ZNCC method analyzes the output speckle field to determine the temperature and salinity. In high-precision and high-sensitivity measurement scenarios including marine environmental monitoring, construction, and biochemical inspection, it has significant development potential and application value.

2. Operation principle

The Vernier effect was first applied to measuring equipment like Vernier calipers and barometers to improve the resolution of length measurement. By utilizing the small-scale difference between the main ruler and the Vernier, these instruments can magnify the measured parameters [25].

2.1. Vernier effect

Vernier effect-based optical fiber sensors take advantage of the slight difference in optical path length between two optical fiber interferometers to achieve sensitization. Firstly, the principle of harmonic Vernier effect based on series fiber FPIs is analyzed. In theory, three reflecting surfaces M_1, M_2 and M_3 are formed at the junction of single-mode fiber (SMF), HCF, and EDF. Three reflecting surfaces form three FPI named as air FPI cavity, silica FPI cavity, and hybrid cavity. The total reflection intensity can be expressed as [26,27]:

$$
\begin{aligned}
I(\lambda) &= |A_1 - A_2 \exp(-i\Delta\varphi_1) + A_3 \exp[-i(\Delta\varphi_1 + \Delta\varphi_2)]|^2 \\
&= A_1^2 + A_2^2 + A_3^2 - 2A_1A_2 \cos\Delta\varphi_1 - 2A_2A_3 \cos\Delta\varphi_2 + 2A_1A_3 \cos(\Delta\varphi_1 + \Delta\varphi_2)
\end{aligned}
\tag{1}
$$

where A_1, A_2, and A_3 represent the amplitudes of the three reflectors respectively. Among them, the transmission phase difference of air-FPI and silica-FPI is respectively expressed as:

$$
\Delta\varphi_1 = \frac{4\pi}{\lambda} n_1 L_1
\tag{2}
$$

$$
\Delta\varphi_2 = \frac{4\pi}{\lambda} n_2 L_2
\tag{3}
$$

where λ is the wavelength of free space light. n_1 and n_2 are the effective gain coefficients FPI and silica-FPI for modes of propagation in air, respectively. L_1 and L_2 are the cavity lengths of air-FPI and silica-FPI, respectively.

The free spectral range (FSR) of the FPI can be defined as:

$$
FSR = \frac{\lambda^2}{2nL}
\tag{4}
$$

where n represents the refractive index of the propagating medium. The FSR of the envelope is expressed as [8]:

$$
FSR_{envelope} = \frac{FSR_1 \times FSR_2}{|FSR_1 - FSR_2|}
\tag{5}
$$

Compared with the sensing performance of the individual sensor interferometers that make up the system, the Vernier envelope has an amplified sensing capability. The magnification factor is represented by, which is an important parameter for connecting Vernier envelope modulation and interference fringes. The amplification factor M is defined as expressed as [25] :

$$
M = \frac{FSR_{envelope}}{FSR_2} = \frac{FSR_1}{|FSR_2 - FSR_1|}
\tag{6}
$$

Consequently, even slight changes in the external environment will induce a wavelength displacement that surpasses any individual interference spectrum, thereby significantly enhancing sensing sensitivity [28]. Nevertheless, there exists a trade-off between the magnification factor and the Vernier envelope as an increased magnification amplifies the envelope of the Vernier effect, posing challenges for accurate detection [25]. Simultaneously, an elevated M leads to a reduced linear measurement range of the sensor [29].

In this study, the structure is used to measure temperature and salinity respectively. For temperature measurements, silica-FPI dominates and is a wavelength-sensitive mechanism. [14].

In the temperature experiment, compared with air-FPI, the temperature change of silica-FP is dominant. For silica-FPI, the thermal expansion coefficient and thermoluminescence coefficient are 5.5×10^{-7} /°C and 1.0×10^{-5} /°C [14,26], respectively. When the temperature changes, the thermal-optical coefficient is dominant. Therefore, EDF with a higher thermal-optical coefficient is selected in the experiment to improve the temperature sensitivity of the system [30]. For salinity measurements, the reflectance of M_3 and R_3 dominates, and it is an intensity-sensitive mechanism. So, the intensity of the reflected light varies with the salinity of the liquid.

2.2. Principle of optical fiber specklegrams fundamental

The statistical information of the speckle pattern represents the sensing information, and the light intensity measured by CCD or CMOS can be expressed by the following [31]:

$$I(x, y) = = \sum_{m=0}^{M-1} \sum_{n=0}^{M-1} a_m a_n \exp[j(\varphi_m - \varphi_n)] \tag{7}$$

where a_m and φ_n are amplitude and phase of the m-th mode and n-th mode, respectively.

The structure employed has a hybrid sensing mechanism. The speckle distribution represents the relationship between the various modes of light propagation in the fiber. It is similar to the way that the simulated XY-axis electric field distribution is sensed in silicon-based photonics [32]. When the temperature changes, the envelope of the combined spectrum will shift, which can be regarded as a wavelength modulation sensor. When the salinity changes, the light intensity will change, which can be regarded as an intensity modulation sensor. External physical quantities such as fiber length, numerical aperture, laser power, wavelength, and emission conditions are kept unchanged during the experiment. The change of light intensity and phase of different wavelengths will cause the change of speckle, so the temperature and salinity can be measured by speckle.

2.3. Operation principle of zero means normalized cross correlation

To provide quantifiable measures between different speckle patterns, the ZNCC algorithm is used. It is mainly used in image registration, target tracking, and other applications. Among them, ZNCC eliminates the influence of brightness and contrast by normalizing the mean and standard deviation of the matched image. Therefore, using the ZNCC algorithm can improve the accuracy and robustness of image matching. ZNCC is expressed by the formula [17,33]:

$$Z_{ref} = \frac{\iint (I_0 - \overline{I_0})(I_{ref} - \overline{I_{ref}})dxdy}{\left[\iint (I_0 - \overline{I_0})^2 dxdy \iint (I_{ref} - \overline{I_{ref}})^2 dxdy\right]^{1/2}} \tag{8}$$

I_0 and I_{ref} is the pixel intensity detected speckle pattern of reference and test images, respectively. $\overline{I_0}$ and $\overline{I_{ref}}$ are the average intensities. Where $0 \leq Z_{ref} \leq 1$.

3. Experimental systems sensor structure and principle of measurement

The Vernier effect-based FP sensing structure consists of two parts. A small section of HCF and EDF are fused successively at the end of SMF. The process of cutting the HCF and EDF is carried out under a microscope. Figure 1(a) is the microscopic image of the FP cavity of the SMF-HCF-EDF structure. Due to the mismatch between the refractive index of the fiber core and the air, three reflective surfaces are formed, corresponding to M_1, M_2 and M_3 in the figure respectively. The measured cavity lengths of the two FPIs cavities are $L_1 = 192.77\,\mu m$ and $L_2 = 240.85\,\mu m$, respectively. As is shown in Fig. 1(b), the SEM image of the fiber cross-section of HCF. The diameter of the HCF is about $126.88\,\mu m$, and the diameter of the air hole is about

40.17 µm. In theory, this structure has three reflecting surfaces, forming three FPI, and a hybrid sensing mechanism can be obtained: wavelength sensitive to temperature and intensity sensitive to refractive index (RI) [14].
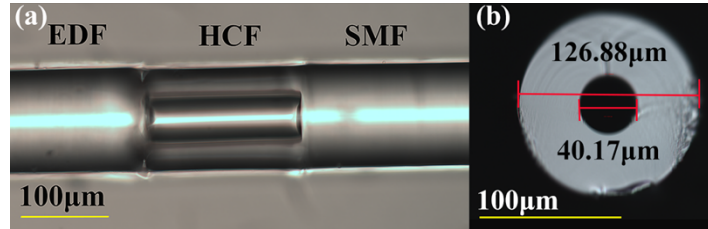

Fig. 1. (a) Microscopic image of FPIs based on the Vernier effect. (b) microscopic image of the cross-section of HCF.
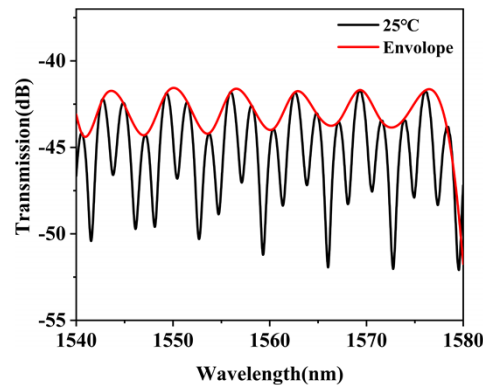

Fig. 2. Optical fiber temperature sensor test system based on OSA.

Figure 2 shows the spectrum experiment system based on the Vernier effect of the proposed sensor. The broadband light source (BBS) transmits the incident light to the sensing structure through the circulator, and the reflection spectrum is recorded by the OSA (Yokogawa, AQ6370D). Figure 2 shows the reflection spectrum and envelope of the Vernier effect-based FPI structure fiber optic sensor at 25 °C, and the periodic envelope can be seen.
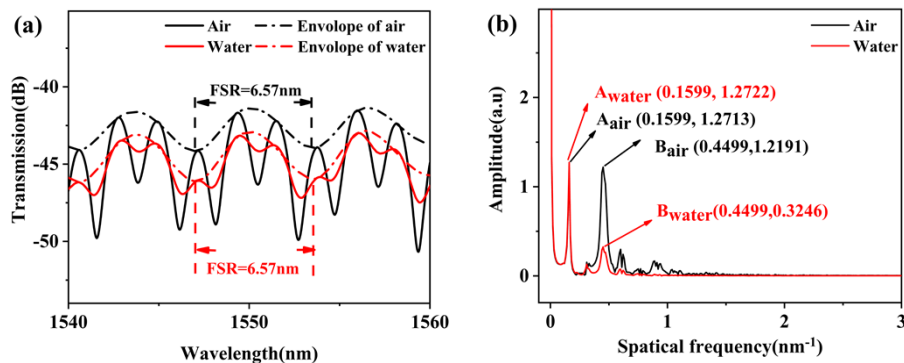

Fig. 3. (a) The spectrum of cascaded FPI structures in air (black) and water (red). (b) Spatial frequency of the FPIs fiber structure.

Figure 3(a) shows the spectrum of the proposed structure in air and water. At the wavelength of 1550 nm, the FSR value of the spectrum in air and water is 6.57 nm. The trend of spectral variation can be obtained obviously when the RI changes. By comparison, it can be seen that when the ambient RI changes, the output power changes with it, while the wavelength position remains almost unchanged. This is in accordance with the theoretical analysis in Section 2.
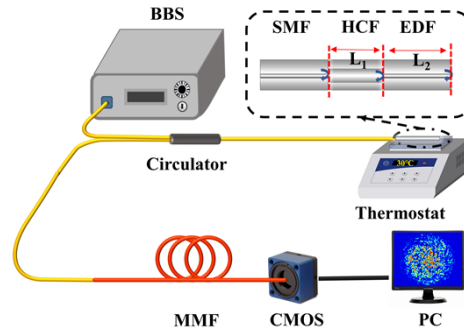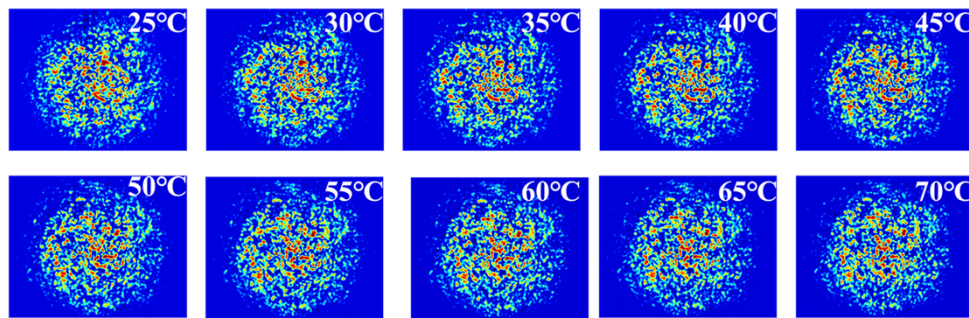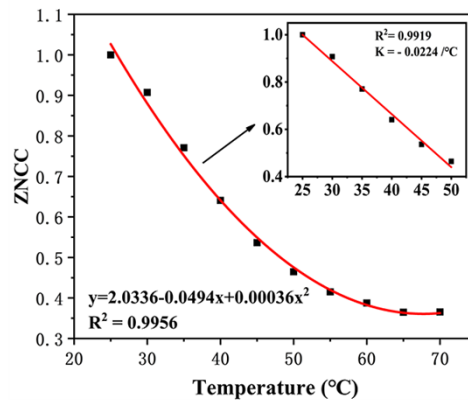

Fig. 4. Schematic diagram of speckle sensor based on vernier effect structure. BBS: broadband light source.

Fig. 5. (a) Speckle pattern at temperatures between 25 °C ~ 70 °C. (b) Relationship between temperature and ZNCC value of speckle (25°C as reference value).

The proposed sensor has three FPIs cavities. The air cavity is only affected by temperature, while the mixing cavity is affected by temperature and salinity of its end face. Therefore, using the reflection spectrum of the hybrid FPIs sensor, the two measurements can be separated by fast Fourier transform (FFT).

By performing FFT on the output spectrum of Fig. 3(a), the spatial spectrum of the cascade FPIs structure is obtained, as shown in Fig. 3(b). The peaks are marked with A, and B respectively. It can be seen from Fig. 3(b), that when the RI changes, the position of the spatial frequency remains unchanged, but the amplitude value of peak B changes. It means that the existing mode is unchanged, the intensity of the first-order cladding mode is almost not affected by the external RI, and the intensity of the second-order cladding mode decreases with the increase of the RI.

In the first section of HCF with a length of 192.17 µm, the corresponding frequency is 0.1600 nm^{-1}, close to the frequency peak A = 0.1599 nm^{-1}. The second EDF has a length of 240.85 µm, but the peak is weak. A corresponding frequency of the total length is equal to 0.4502 nm^{-1}, which is close to the frequency peak B = 0.4499 nm^{-1}. So, the FPIs consist of two cascading structures: air-cavity and hybrid-cavity.

The schematic diagram of the speckle sensor based on the Vernier effect structure is shown in Fig. 4. The BBS transmits the incident light to the sensing structure through the circulator. The reflectance spectrum passes through a MMF with a length of 35 cm (core $400 \pm 5 \mu m$, cladding $440 \pm 5 \ \mu m$, NA = 0.22 ± 0.02), and speckles are formed at the end of the MMF. Speckles are received by CMOS camera (CINOGY Technologies, CinCam CMOS-1201-IR). The experiment is carried out in a dark room, and the experimental devices are placed on the shock-proof test bench to reduce the influence of the external environment during the experiment. To stimulate more higher-order modes and thus enhance the effect of interference, a mismatch welding method is adopted between SMF and MMF [20]. The image data is collected by the data-receiving module in the computer.

4. Results and discussions

4.1. Temperature sensing experiments

The temperature sensing experiment is as follows: The FPI structure is placed in a thermostat with a temperature range of 25 °C ~ 70 °C, a step size of 5 °C, and an accuracy of ± 0.1 °C. After the temperature stabilizes for 5 mins, the data collected by CMOS is processed using the ZNCC algorithm. To expand the practicability of temperature measurement, the starting point of the measurement is 25°C. In addition, ZNCC can change the dynamic range by adjusting the reference image. Therefore, the ZNCC uses 25 °C image information as a reference value when processing data.

Figure 5(a) shows speckle pattern at temperatures between 25 °C ~ 70 °C. It can be concluded that the temperature speckle patterns have better randomness. When the temperature changes, the excitation and energy distribution of the model will change, resulting in corresponding fluctuations in the speckle pattern. As shown in Fig. 5(b), when the temperature rises from 25 °C to 70 °C, the ZNCC value decreases from 1 to 0.3654. As the temperature increases, the relationship between ZNCC and temperature can be described by second-order polynomial fitting analysis. The fitting curve can be expressed as $y = 2.0336 - 0.0494x + 0.00036x^2$. And the R-square value reaches 0.9956. The data is further analyzed in the range of 25 ~ 50 °C. The experimental results show that the sensor has a relatively stable linear relationship in the dynamic range of 25 ~ 50 °C. In the case of good linearity, the fitting formula becomes a first-order function, and the process of inverse derivation of monitoring parameters through the formula is simpler, thus simplifying the calculation. The ZNCC value has a linear relationship with temperature in this interval, and the temperature sensitivity of the sensor is - 0.0224 /°C with the R-square value is 0.9919. For the proposed cascaded FPI structures sensor, the amplification factor M can be improved by changing the length of each FP in a certain range.
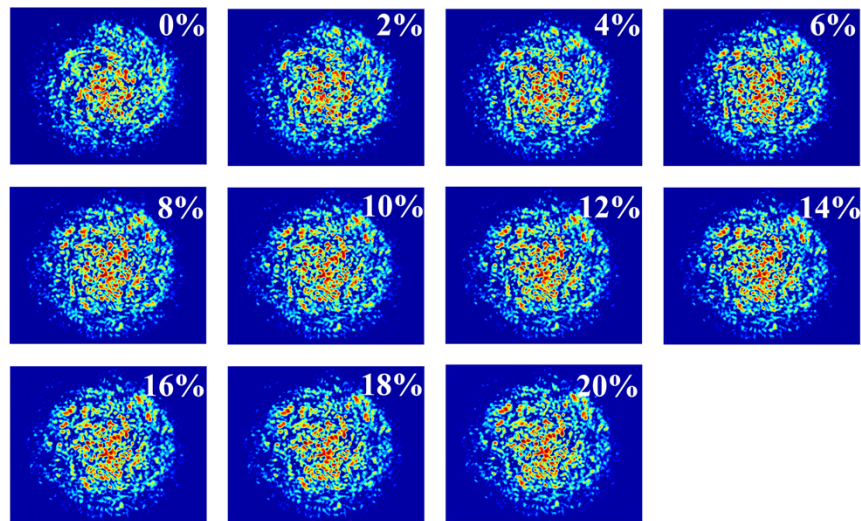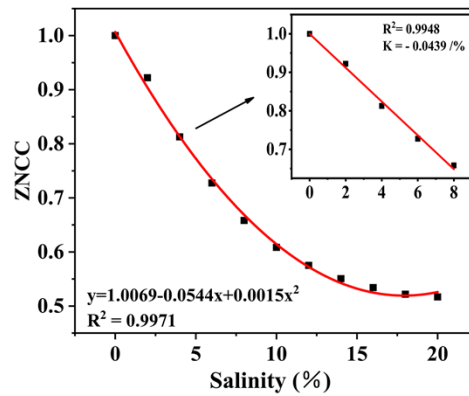
Fig. 6. (a) speckle pattern with salinity in the range of 0% ~ 20%. (b) Relationship between salinity and ZNCC value of speckle (0% as reference value).

4.2. Salinity sensing experiments

The salinity speckle sensing experiment uses the same sensor. The salt solution with a mass fraction of 0% ∼ 20% is added successively, and the speckle data is recorded after being stabilized for 3 mins. The reference pattern is recorded in pure water and used as a reference pattern for ZNCC speckles. Figure 6 shows the results of speckle sensing experiments under different salinity.
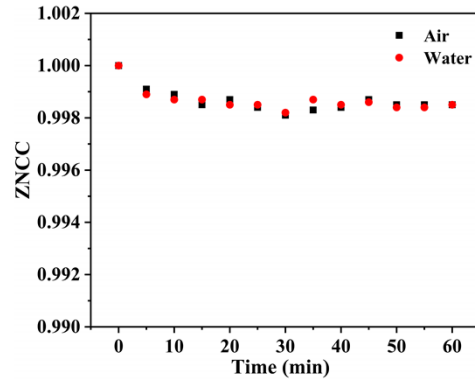

Fig. 7. Temperature stability experiments of speckle based on Vernier effect in air (black) and water(red).

As shown in Fig. 6(b), when salinity increases from 0% to 20%, the ZNCC value decreases from 1 to 0.5126. With the increase of salinity, the relationship between ZNCC and salinity can be described by second-order polynomial fitting analysis. The fitting curve can be expressed as $y = 1.0069 - 0.0544x + 0.0015x^2$. And the R-square value reaches 0.9971. The data are further analyzed in the salinity range of 0% ∼ 8%. At low concentrations, it can be approximated as a linear change. The salinity to be measured can be obtained by a simple first-order equation. The ZNCC value has a linear relationship with salinity in this interval, and the salinity sensitivity of the sensor is −0.0439 /% with the R-square value is 0.9948. Salinity sensitivity can be improved by adjusting the reflectivity of the end face (intensity demodulation).

4.3. Stability test experiments

To further analyze the stability of the proposed sensor, the FPIs are placed in deionized water and air respectively for stability experiments. The speckle image data are recorded every 5 mins at 25 °C during the experiment. Based on the initial time after stabilization, the ZNCC algorithm is used to process the speckle image at each time. As shown in Fig. 7, the experimental results show that the mean value for air and water is 0.99868 and 0.99866, and the population standard deviation is 4.7×10^{-4} and 4.2×10^{-4}, respectively. The cause of the fluctuation may be the slight noise caused by the vibration of the thermostatic radiator. The interference of the external environment can be reduced by packaging technology. Therefore, the sensor has good stability and can be used for temperature and salinity detection.

4.4. Discussions

Vernier effect can improve the sensitivity by adjusting FSR close but not equal, speckle is also sensitive to changes in the external environment. In the experiment, an FPI structure with strong temperature stability is used to improve the practicability of the sensor system. Sensors based on speckle sensing must be installed in a stable environment to isolate the effects of the external environment. Therefore, packaging the speckle test system and sensing unit to improve the stability of the system is also the future development direction.

The sensor uses a cascade FP structure, which has the advantage of being tested as a probe. Therefore, the performance of long-distance testing is verified by experiments. Standard SMF of 0 Km, 5 Km, and 10 Km were connected to the front end of the sensor. The optical losses measured at 5 Km and 10 Km are 0.27 dBm and 0.59 dBm, and the ZNCC values of speckle are 0.9884 and 0.9696, respectively. It can be seen that with the increase of the propagation distance, the optical power decreases and the ZNCC value decreases. The sensor has the potential for long-distance transmission and the sensing experiment should be carried out after calibration at the same distance.

Previous work has shown that applying the Vernier effect to fiber optic interferometers is a way to improve the sensitivity and resolution of fiber optic sensors [9,14]. Sensitivity can also be improved by sensitizing materials [13,30]. Compared with the method of tracking the movement of the spectrum envelope in OSA, the speckle sensing method is more convenient for processing the Vernier effect image. The requirement for additional signal processing to extract the wavelength shift of the Vernier envelope from the spectrum is eliminated [34]. Speckle sensing measurement range can be extended by selecting a new reference pattern for the ZNCC. It can simplify the theoretical analysis and expand the practical application [33]. To improve measurement accuracy, periodic calibration is required to compensate for final temperature and light source stability [21].

In this study, speckle demodulation is used to demodulate the Vernier effect in optical fiber sensing. Temperature change causes spatial frequency shift, and salinity change causes intensity change in the spatial spectrum [16]. So, speckle sensing experiments are carried out on temperature and salinity respectively. For the fiber crosstalk problem, it is possible to decompose the temperature and salinity variables by combining neural networks, machine learning [5], and other technologies [24,35–37] with image processing methods. The future work will focus on the realization of synchronous demodulation and real-time monitoring of two parameters. The effective combination with integrated circuit can solve the stability and miniaturization problems of the system [38]. At the same time, the practical application of the system can be improved through the combination of effective packaging technology [39].

5. Conclusion

The demodulation of temperature and salinity is done with speckle in this study, which also introduces a probe-type optical fiber sensor with an FPI structure that uses the Vernier effect. The demodulation by speckle method solves the inconsistent problem that the envelope measurement results of tracking different upper envelopes or lower envelopes. A little piece of HCF and EDF fused to the end of SMF to create a series FPI structure that makes up the sensor. The sensor head with a total length of 0.434 mm achieves a temperature detection sensitivity of $-0.0224 / \,°C$ and a salinity detection sensitivity of $-0.0439 /\%$. High-resolution and high-speed measurement requirements can both be met by the demodulation method based on speckle. It is expected that the demodulation scheme can be used to measure the demodulation of various sensors based on the Vernier effect, such as RI, stress, displacement, and vibration.

References

1. G. Zhou and R.-H. Zhang, "Structure and evolution of decadal spiciness variability in the North Pacific during 2004–20, revealed from Argo observations," Adv. Atmos. Sci. **39**(6), 953–966 (2022).

2. R. Min, Z. Liu, and L. Pereira, *et al.*, "Optical fiber sensing for marine environment and marine structural health monitoring: A review," Opt. Laser Technol. **140**, 107082 (2021).

3. Y. Liu, X. Li, and Y.-n. Zhang, *et al.*, "Fiber-optic sensors based on Vernier effect," Measurement **167**, 108451 (2021).

4. J. Hu, L. Shao, and G. Gu, *et al.*, "Dual Mach–Zehnder Interferometer Based on Side-Hole Fiber for High-Sensitivity Refractive Index Sensing," IEEE Photonics J. **11**(6), 1–13 (2019).

5. A. G. Leal-Junior, V. Campos, and C. Díaz, *et al.*, "A machine learning approach for simultaneous measurement of magnetic field position and intensity with fiber Bragg grating and magnetorheological fluid," Opt. Fiber Technol. **56**, 102184 (2020).

6. W. Lin, H. Liu, and C. Yang, *et al.*, "Fibre-optic salinity sensor based on multimode fibre specklegram analysis," Meas. Sci. Technol. **32**(11), 115110 (2021).

7. X. Fang, W. Zhang, and J. Li, *et al.*, "Signal processing assisted Vernier effect in a single interferometer for sensitivity magnification," Opt. Express **29**(8), 11570–11581 (2021).

8. W. Zenghui, J. Shaocui, and Y. peng, *et al.*, "High-sensitivity and high extinction ratio fiber strain sensor with temperature insensitivity by cascaded MZI and FPI," Opt. Express **31**(5), 7073–7089 (2023).

9. L.-Y. Shao, Y. Luo, and Z. Zhang, *et al.*, "Sensitivity-enhanced temperature sensor with cascaded fiber optic Sagnac interferometers based on Vernier-effect," Opt. Commun. **336**, 73–76 (2015).

10. S. Liu, G. Lu, and D. Lv, *et al.*, "Sensitivity enhanced temperature sensor with cascaded Sagnac loops based on harmonic Vernier effect," Opt. Fiber Technol. **66**, 102654 (2021).

11. D. N. Wang, X. L. Cui, and H. Zhang, *et al.*, "Ultrasensitive Strain Sensing by Using Two Parallel Structured Fabry–Perot Interferometers in Cascaded Connection," J. Lightwave Technol. **39**(5), 1504–1508 (2021).

12. Y. Yang, Y. Wang, and Y. Zhao, *et al.*, "Sensitivity-enhanced temperature sensor by hybrid cascaded configuration of a Sagnac loop and a F-P cavity," Opt. Express **25**(26), 33290 (2017).

13. W. Yang, R. Pan, and L. Zhang, *et al.*, "Highly sensitive fiber-optic temperature sensor with compact hybrid interferometers enhanced by the harmonic Vernier effect," Opt. Express **31**(9), 14570–14582 (2023).

14. W. Zhang, H. Li, and L. Zhu, *et al.*, "Dual-Parameter Optical Fiber Probe Based on a Three-Beam Fabry-Perot Interferometer," IEEE Sens. J. **21**(4), 4635–4643 (2021).

15. C. R. Liao, T. Y. Hu, and D. N. Wang, "Optical fiber Fabry-Perot interferometer cavity fabricated by femtosecond laser micromachining and fusion splicing for refractive index sensing," Opt. Express **20**(20), 22813–22818 (2012).

16. H. Choi, G. Mudhana, and K. S. Park, *et al.*, "Cross-talk free and ultra-compact fiber optic sensor for simultaneous measurement of temperature and refractive index," Opt. Express **18**(1), 141–149 (2010).

17. T. D. Cabral, E. Fujiwara, and S. C. Warren-Smith, *et al.*, "Multimode exposed core fiber specklegram sensor," Opt. Lett. **45**(12), 3212–3215 (2020).

18. E. Fujiwara, L. E. d. Silva, and T. D. Cabral, *et al.*, "Optical Fiber Specklegram Chemical Sensor Based on a Concatenated Multimode Fiber Structure," J. Lightwave Technol. **37**(19), 5041–5047 (2019).

19. E. Fujiwara and T. Cabral, "Optical fiber specklegram sensor for multi-pointcurvature measurements," Appl. Opt. **61**(23), 6787–6794 (2022).

20. W. Chen, F. Feng, and D. Chen, *et al.*, "Precision non-contact displacement sensor based on the near-field characteristics of fiber specklegrams," Sens. Actuators, A **296**, 1–6 (2019).

21. E. Fujiwara, F. D. Paula, and Y. T. Wu, *et al.*, "Optical fiber tactile sensor based on fiber specklegram analysis," in *2017 25th Optical Fiber Sensors Conference (OFS), Jeju, Korea (South)*, 2017, 1–4.

22. A. G. Leal-Junior, A. Frizera, and C. Marques, *et al.*, "Optical Fiber Specklegram Sensors for Mechanical Measurements: A Review," IEEE Sens. J. **20**(2), 569–576 (2020).

23. Y. Guan, J. Yang, and B. Yin, *et al.*, "Study of the Sensitivity Limit of Vernier Effect and a Novel Tracking Method of Vernier Envelope," IEEE Photonics Technol. Lett. **35**(2), 77–80 (2023).

24. T. Wang, Y. Li, and J. Tao, *et al.*, "Deep-learning-assisted fiber Bragg grating interrogation by random speckles," Opt. Lett. **46**(22), 5711–5714 (2021).

25. Y. Chen, L. Zhao, and S. Hao, *et al.*, "Advanced Fiber Sensors Based on the Vernier Effect," Sensors **22**(7), 2694 (2022).

26. Y. Wu, Y. Zhang, and J. Wu, *et al.*, "Fiber-Optic Hybrid-Structured Fabry–Perot Interferometer Based On Large Lateral Offset Splicing for Simultaneous Measurement of Strain and Temperature," J. Lightwave Technol. **35**(19), 4311–4315 (2017).

27. Z. Yizheng, K. L. Cooper, and G. R. Pickrell, *et al.*, "High-temperature fiber-tip pressure sensor," J. Lightwave Technol. **24**(2>), 861–869 (2006).

28. G. An, L. Liu, and P. Hu, *et al.*, "Probe type TFBG-excited SPR fiber sensor for simultaneous measurement of multiple ocean parameters assisted by CFBG," Opt. Express **31**(3), 4229–4237 (2023).

29. R. Pan, W. Yang, and L. Li, *et al.*, "High-sensitive fiber-optic pressure sensor based on Fabry-Perot interferometer filled with ultraviolet glue film and Vernier effect," Opt. Fiber Technol. **67**, 102710 (2021).

30. W. H. Lin, F. Zhao, and L. Y. Shao, *et al.*, "Temperature Sensor Based on Er-Doped Cascaded-Peanut Taper Structure In-Line Interferometer in Fiber Ring Laser," IEEE Sens. J. **21**(19), 21594–21599 (2021).

31. D. Halpaap, J. Tiana-Alsina, and M. Vilaseca, *et al.*, "Experimental characterization of the speckle pattern at the output of a multimode optical fiber," Opt. Express **27**(20), 27737–27744 (2019).

32. K. Xu, "Silicon electro-optic micro-modulator fabricated in standard CMOS technology as components for all silicon monolithic integrated optoelectronic systems," J. Micromech. Microeng. **31**(5), 054001 (2021).

33. P. Guo, H. Liu, and Z. Zhou, *et al.*, "Spatially Modulated Fiber Speckle for High-Sensitivity Refractive Index Sensing," Sensors **23**(15), 6814 (2023).

34. A. Gomes, H. Bartelt, and O. Frazão, "Optical Vernier Effect: Recent Advances and Developments," Laser Photonics Rev. **15**, 1 (2021).

35. L. Nguyen, V. Nguyen, and G. Carneiro, *et al.*, "Sensing in the presence of strong noise by deep learning of dynamic multimode fiber interference," Photonics Res. **9**(4), B109 (2021).

36. G. Li, Y. Liu, and Q. Qin, *et al.*, "Deep learning based optical curvature sensor through specklegram detection of multimode fiber," Opt. Laser Technol. **149**, 107873 (2022).

37. M. Wei, G. Tang, and J. Liu, *et al.*, "Neural Network Based Perturbation-Location Fiber Specklegram Sensing System Towards Applications With Limited Number of Training Samples," J. Lightwave Technol. **39**(19), 6315–6326 (2021).

38. K. Xu, L. Huang, and Z. Zhang, *et al.*, "Light emission from a poly-silicon device with carrier injection engineering," Mater. Sci. Eng., B **231**, 28–31 (2018).

39. D. B. Duraibabu, G. Leen, and D. Toal, *et al.*, "Underwater Depth and Temperature Sensing Based on Fiber Optic Technology for Marine and Fresh Water Applications," Sensors **17**(6), 1228 (2017).